Supplementary Information

Self-Powered VO_2 Phase Transition Based on Triboelectric Nanogenerator

Tianrui Dang,‡[ab] Junqing Zhao,‡[bc] Jianhua Zeng,[bd] Tianzhao Bu,[e] Jiaodi Li,[bd] Yiming Dai,[ab] Zefang Dong,[bc] Yuan Feng,[bd] Yuanfen Chen,*[a] and Chi Zhang,*[abcde]

[a] School of Mechanical Engineering, Guangxi University, Nanning 530004, P. R. China

[b] Beijing Key Laboratory of Micro-Nano Energy and Sensor, Center for High-Entropy Energy and Systems, Beijing Institute of Nanoenergy and Nanosystems, Chinese Academy of Sciences, Beijing 101400, P. R. China

[c] School of Nanoscience and Engineering, University of Chinese Academy of Sciences, Beijing 100049, P. R. China

[d] Center on Nanoenergy Research, Institute of Science and Technology for Carbon Peak & Neutrality, Key Laboratory of Blue Energy and Systems Integration (Guangxi University), Education Department of Guangxi Zhuang Autonomous Region, School of Physical Science & Technology, Guangxi University, Nanning 530004, P. R. China

[e] School of Mechanical Science & Engineering, Huazhong University of Science and Technology, Wuhan 430074, P. R. China

‡ Tianrui Dang and Junqing Zhao contributed equally to this work.

* Corresponding author:
E-mail addresses: yuanfenchen@gxu.edu.cn (Yuan F. Chen), czhang@binn.cas.cn (C. Zhang)

Supplementary note 1: Working mechanism and electrical characterization of the contact-separation mode TENG

The working mechanism of the contact-separation TENG is depicted in **Figure S1a**. In the initial phase, the upper Cu film is in contact with the lower PTFE film. Given their opposite frictional electrical polarity, the Cu and PTFE films acquire positive and negative charges, respectively (**Figure S1a(i)**). As they separate, the potential of the Cu film increases and causes the flow of electrons from the lower Cu electrode to the upper Cu film through an external circuit (**Figure S1a(ii)**). When completely separated, all electrons flow to the upper Cu electrode (**Figure S1a(iii)**). Following the Cu film approaches the PTFE film again, the electrons flow from the upper Cu film to the lower Cu electrode through the external circuit (**Figure S1a(iv)**). With the continuous contact-separation motion of Cu film, electrons flow back and forth between the two electrodes and generate an AC output in the external circuit. When the TENG operates with a displacement distance of 2 mm, the V_{OC} is approximately 48 V (**Figure S1b**), and the I_{SC} is about 3 μA (**Figure S1c**).

Supplementary note 2: Impedance analysis of the ionic gel layer

To investigate the resistance-capacitive properties of the ionic gel by impedance spectroscopy, employing a typical metal-insulator-metal (MIM) resistor-capacitor (RC) model,[1-6] as shown in **Figure S2**. The resistive-capacitive parameters of the ionic gel are measured by loading an AC voltage with a frequency from 20 Hz to 20 MHz (**Figure S2b-d**). **Figure S2b** shows that the capacitance of the ionic gel exceeds 100 nF cm^{-2} at a low frequency of 20 Hz, and is lower than 0.1 nF cm^{-2} at a high frequency of 0.1 MHz. The phenomenon is attributable to the electrode/ionic gel interface, where not only is an electric double layer formed, but faradaic impedance also arises (stemming from active ions in the electrolyte, undergoing redox reactions). These results indicate that the ionic gel is subject to simultaneous ion diffusion and electrochemical control. The phase angles of the ideal capacitor and resistor are −90° and 0°, respectively, which means the −45° phase angle is the transition point between capacitance characteristic and resistance characteristic. **Figure S2c** shows the relationship between the phase angle of the ionic gel RC and the loaded frequency. When the frequency is less than 0.03 MHz, the ionic gel exhibits resistive behavior, which gradually changes to capacitive behavior as the frequency increases. The result is due to the formation of a

thicker diffusion layer in the low-frequency region, which leads to the appearance of Warburg impedance during ion diffusion (mass transfer). Conversely, in the high-frequency region, the excessively short period for variation impedes timely ion transfer, thus resulting in domination by electrochemical reactions (charge transfer). The Nyquist plot, which graphs the real and imaginary parts of the ion gel impedance at different frequencies (**Figure S2d**), validates this process. In the high-frequency region, the behavior of ionic gel is controlled by electrochemical reactions, appearing as a semicircle. In the low-frequency region, it is controlled by diffusion, appearing as a positive slope line. The findings demonstrate that the ionic gel works similarly to a resistor-capacitor unit, with its behavior determined by a combination of ion diffusion and electrochemical control.

Supplementary note 3: Working mechanism and electrical characterization of the raindrop TENG

The working mechanism of a single raindrop TENG is depicted in **Figure S6a**. Initially, when the first raindrop lands on the PTFE surface and rolls, the PTFE film acquires negative charges due to the difference in electronegativity, and these charges persist for an extended period. Thus, the two Al electrodes in contact with the PTFE induce positive charges (**Figure S6a(i)**). As a raindrop falls on the left electrode, the potential of the left electrode becomes higher than that of the right electrode, causing a flow of electrons from the right electrode to the left electrode through an external circuit (**Figure S6a(ii)**). When the raindrop rolls from the left to the right electrode, the corresponding electrons flow from the left to the right electrode through the external circuit (**Figure S6a (iii, iv)**). Once the raindrop rolls off the TENG, the potential difference drives the flow of free electrons from the right electrode back to the left electrode through the external circuit, returning to the initial state. This repeated contact and separation between raindrops and the PTFE film surface generate continuous AC output. The integrated array raindrop TENG exhibits a V_{OC} of approximately 70 V (**Figure S6b**) and an I_{SC} of about 5 μA (**Figure S6c**).

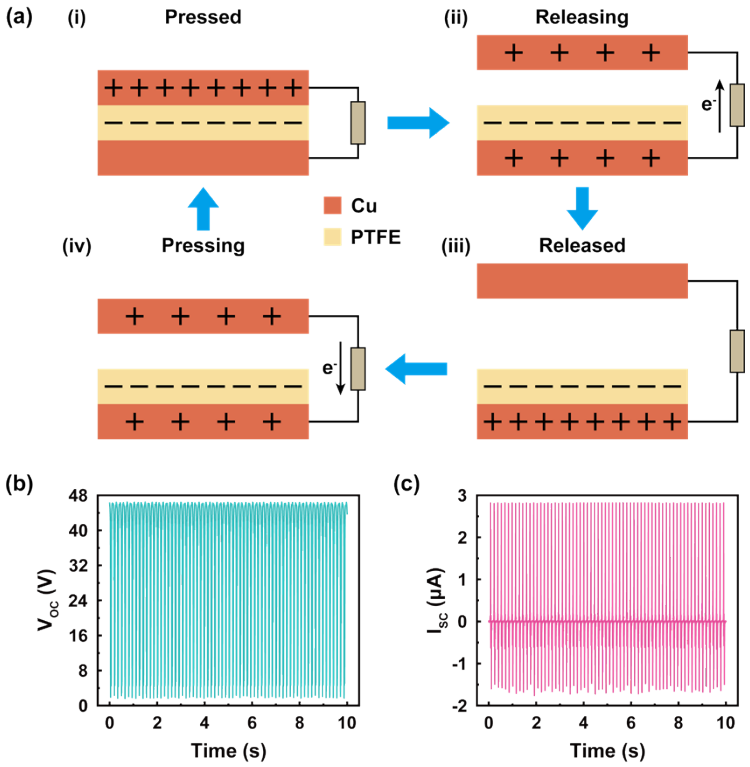

Figure S1. Working mechanism and electrical characterization of the contact-separation mode TENG. (a) The working mechanism of the contact-separation mode TENG. (b) Open circuit voltage (V_{OC}) of the contact-separation mode TENG. (c) Short circuit current (I_{SC}) of the contact-separation mode TENG.

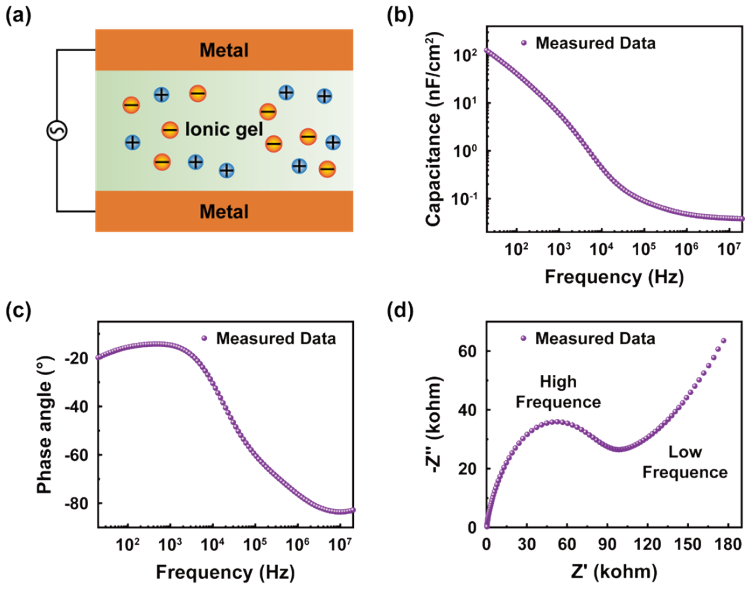

Figure S2. Impedance analysis of the ionic gel layer. (a) Typical MIM structure diagram of the ionic gel layer. (b) The functional relationship between the capacitance of the ionic gel layer and the frequency of applied AC. (c) The functional relationship between the phase angle of the ionic gel layer and the frequency of applied AC. (d) Nyquist plot of the ionic gel layer.

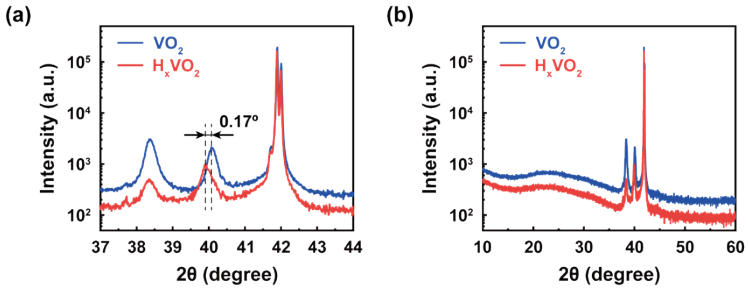

Figure S3. X-ray diffraction analysis of VO_2 and H_xVO_2 thin films. (a) X-ray diffraction angle deviation of VO_2 and H_xVO_2 thin films. (b) X-ray diffraction scanning of VO_2 and H_xVO_2 thin films from 10 to 60 degrees.

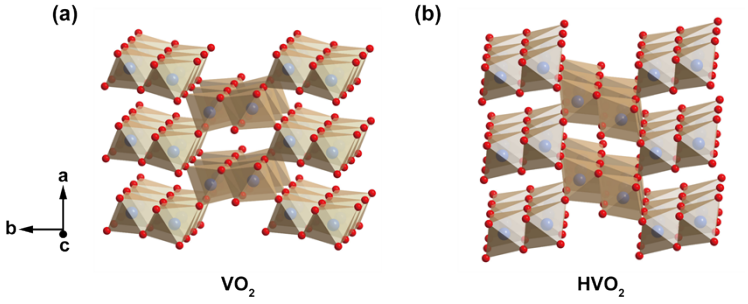

Figure S4. Schematic of the lattice structure.[7] Lattice structures of (a) VO_2 and (b) HVO_2.

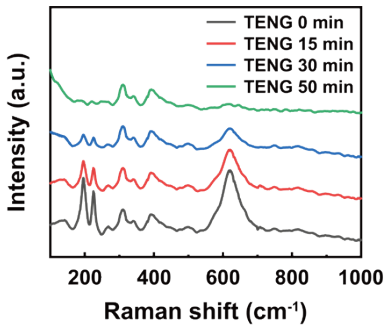

Figure S5. Raman spectra of phase transition regions with different operating times of the TENG.

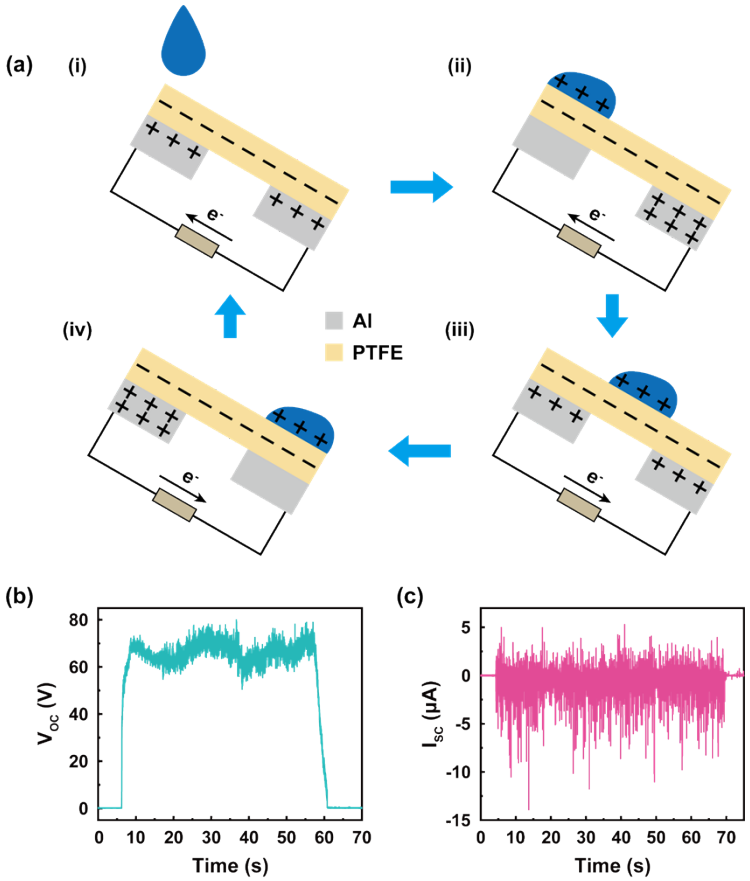

Figure S6. Working mechanism and electrical characterization of the raindrop TENG. (a) The working mechanism of the raindrop TENG. (b) Open circuit voltage (V_{OC}) of the integrated array raindrop TENG. (c) Short circuit current (I_{SC}) of the integrated array raindrop TENG.

References

1. C. S. Wang, A. J. Appleby and F. E. Little, Electrochemical impedance study of initial lithium ion intercalation into graphite powders, *Electrochimica Acta*, 2001, **46**, 1793-1813.
2. K. H. Lee, S. P. Zhang, T. P. Lodge and C. D. Frisbie, Electrical Impedance of Spin-Coatable Ion Gel Films, *J. Phys. Chem. B*, 2011, **115**, 3315-3321.
3. S. Y. Wang, M. Y. Yan, Y. Li, C. Vinado and J. H. Yang, Separating electronic and ionic conductivity in mix-conducting layered lithium transition-metal oxides, *J. Power Sources*, 2018, **393**, 75-82.
4. Y. F. Meng, J. Q. Zhao, X. X. Yan, C. L. Zhao, S. S. Qin, J. H. Cho, C. Zhang, Q. J. Sun and Z. L. Wang, Mechanosensation-Active Matrix Based on Direct-Contact Tribotronic Planar Graphene Transistor Array, *ACS Nano*, 2018, **12**, 9381-9389.
5. X. X. Yang, J. Han, J. R. Yu, Y. H. Chen, H. Zhang, M. Ding, C. K. Jia, J. Sun, Q. J. Sun and Z. L. Wang, Versatile Triboiontronic Transistor *via* Proton Conductor, *ACS Nano*, 2020, **14**, 8668-8677.
6. J. H. Zeng, J. Q. Zhao, T. Z. Bu, G. X. Liu, Y. C. Qi, H. Zhou, S. C. Dong and C. Zhang, A Flexible Tribotronic Artificial Synapse with Bioinspired Neurosensory Behavior, *Nano-Micro Letters*, 2023, **15**, 15.
7. H. T. Evans, Jr. and M. E. Mrose, A crystal chemical study of montroseite and paramontroseite*, *Am. Mineral*, 1955, **40**, 861-875.